Kimiabeigi M, Widmer JD, Long R, Gao Y, Goss J, Martin R, Lisle T, Vizan JMS, Michaelides A, Mecrow B.

High-Performance Low-Cost Electric Motor for Electric Vehicles Using Ferrite Magnets.

***IEEE Transactions on Industrial Electronics* 2016, 63(1), 113-122.**

DOI link to article:

http://dx.doi.org/10.1109/TIE.2015.2472517

Date deposited:

15/07/2016

High Performance Low Cost Electric Motor for Electric Vehicles Using Ferrite Magnets

M. Kimiabeigi, J. D. Widmer, R. Long, Y. Gao, J. Goss, R. Martin, T. Lisle, J.M. Soler Vizan, A. Michaelides, B. Mecrow

***Abstract*—Permanent magnet motors with rare earth magnets are amongst the best candidates for high performance applications such as automotive. However, due to their cost and risks relating to security of supply, alternative solutions such as ferrite magnets have recently become popular. In this paper the two major design challenges of using ferrite magnets for a high torque density and high speed application, namely their low remanent flux density and low coercivity, are addressed. It is shown that a spoke type design utilizing a distributed winding may overcome the torque density challenge due to a simultaneous flux concentration and reluctance torque possibility. Furthermore, the demagnetization challenge can be overcome through careful optimization of the rotor structure, with the inclusion of non-magnetic voids on the top and bottom of the magnets. To meet the challenges of the high speed operation an extensive rotor structural analysis has been undertaken, during which electro-magnetics as well as manufacturing tolerances are taken into account. The electromagnetic studies are validated through testing of a prototype, custom built for static torque and demagnetization evaluation. The disclosed motor design surpasses the state of the art performance and cost, merging the theories into a multi-disciplinary product.**

***Index Terms*—Demagnetization, Electric Vehicle (EV), Ferrite Magnets, Finite Element (FE), High Speed, Power Density.**

I. Introduction

Permanent magnet motors may provide higher power density than alternative motor solutions owing to the use of energy dense rare earth magnets. Hence, they are the most popular choice for high efficiency applications with limited packaging space, such as automotive [1]-[4]. Amongst different topologies, the interior permanent magnet (IPM) type is preferred due to its resistance to demagnetization, and possibilities for flux focusing and reluctance torque; improving the torque density as well as increasing the constant power speed range (CPSR) [5]-[8]. Different magnet topologies in the rotor may be selected for different requirements and performance, the most common options being: single layer V-shape as in Toyota Prius [2], double layer V-shape as in Chevrolet Spark [9], Triangular as in Lexus or Nissan leaf [2] and [4], PM assisted synchronous reluctance (PMASynR) as in BMW i3 [10], and recently spoke type as in [11]. On the other hand, the rare earth magnet materials including Nd and Dy elements are expensive, with an unstable price demonstrating significant volatility during 2003-2014, and environmentally unfriendly [12], [13]. As a result, recently published research has been directed at minimizing the use of rare earths or ultimately eliminating them; a review of the techniques has been reported in [14].

One alternative to rare earth magnets is the application of ferrite magnets which are significantly cheaper and unlike the former have shown a stable price over decades. To compensate for the low remanent flux of the ferrite magnets they might be best applied in an IPM topology with a distributed winding stator, where significant reluctance torque can be achieved. Furthermore, the very low coecivity of these magnets makes them susceptible to demagnetization during field weakening and short-circuit conditions. To overcome this, different features of the rotor design need to be carefully considered. In [6] a low speed, high torque density, three layer, U-shape PMASynR topology benefited from both reluctance torque and flux concentration. In this design, the demagnetization withstand capability was enhanced by tapering the flux barriers toward the airgap and increasing the magnets thickness. In [15] a low speed, high torque density, three layer, V-shape PMASynR design was presented and compared against the Toyota Prius performance, [2]. In [16] a conceptual spoke type topology was compared against the Toyota Prius, where it was shown that embedding the magnets into the rotor can mitigate the demagnetization risk; in [17] a similar concept has been employed in a novel radially-split magnet topology and the demagnetization was tested for the peak torque and 20˚ advance angle. In [18] a low speed 16-pole/ 9-phase spoke type ferrite motor was designed and prototyped but no detailed report is available. In [19] a high speed high torque density spoke type design was reported where demagnetization was studied at the maximum current and advance angle for the peak power operation and 105 ˚C magnet temperature; the demagnetization risk was mitigated by reducing the number of turns as well as widening the magnets.

On the structural side, while most reported spoke designs such as those in [16]-[18] use a single piece rotor lamination topology, few designs such as [19] are based on a two-part rotor structure. In the latter, the rotor is composed of

This project is funded by Innovate UK under grant 110130.

ferromagnetic poles held by a non-magnetic support via a so-called fir-tree embodiment; a technology proposed for use in electrical machines since the 1980s [20], to provide sufficient rotor integrity against the high speed centrifugal forces.

This paper addresses and combines the major challenges involved with the design of a high performance ferrite based motor in a systematic way, including: the methods to achieve high power density, demagnetization withstand capability, and rotor integrity at high speeds. First the preference of the spoke type topology over the main alternative, the PMASynR U-shape and V-shape, is investigated. A spoke type design resulting from a multi-physics based optimization is then presented. The electromagnetic performance of this design, with a major focus on demagnetization withstand capability and the associated key design parameters, is studied. Next, the optimization of the structural design and the fir tree with attention to electromagnetic performance (torque maximization and demagnetization mitigation), manufacturing, and reduction of cost by utilizing cheaper materials is explained. Finally a prototype, representative but one-fifth of the stack length of the full machine, is built and tested to validate the torque and demagnetization performance against the theory.

II. Design and Analysis

A. Packaging and Specification

The main requirements of the ferrite based electric motor, specified as part of an all-electric vehicle project, are summarized in Table I. The available motor package including the shaft, housing and cooling is a cylinder with a volume of less than 14 liter, but the aspect ratio, the ratio of outer diameter to the axial length, is flexible. The available volume and required power density is very demanding and almost identical as the rare-earth based design in Nissan leaf [4]. For the ferrite magnet, the grade FB9B is chosen [21]; the remanent flux density, B_r, and coercivity, H_{cj}, are given in Table I.

Throughout this report, peak current (the maximum transient current available from the inverter) is equal to 420 A, rms, and is set as 1 per unit. Furthermore, peak torque value of 270 Nm is set as 1 per unit, and is defined as the maximum average transient torque that is achieved based on 1 per unit peak current.

Table I
Design Requirements for the Ferrite Based Traction Motor.

Gross volume (including cooling and end winding)	< 14 liter
Peak power density per motor volume	>6 kW/liter
Continuous power density per motor volume	>4 kW/liter
Base to top speed ratio	3000 rpm : 15000 rpm
Maximum winding temperature	180 ˚C
Available water cooling options	Only via outer stator frame
Demagnetization withstand capability	Against 3-phase short circuit
Ferrite, B_r at 20˚C/ H_{cj} at -40˚C	0.43 T/ 330 kA/m
Minimum available DC link voltage	400 V

B. PMASynR vs. Spoke Type Topology

Due to the low remanent flux density of the ferrite magnets and the high power density requirement (Table I), the magnet torque needs to be enhanced by flux focusing and/or reluctance torque. One topology allowing this is the PMASynR topology, with 2 or more layers of magnets. An optimized 3-layer U-shape PMASynR is therefore designed, where the stator is comprised of a distributed winding with a slot per pole and phase equal to 1 to maximize the reluctance torque contribution. A rotor with eight poles is selected; this relatively high pole number is chosen in order to reduce the ampere turn seen by each magnet during the short circuit fault, thus reducing the demagnetization risk. However as is shown in Fig. 1(a), by having a high pole number the available space for the magnets is too limited to allow magnets to be placed in the inclined layers. This means that the opportunity for increased torque due to flux focusing is lost. To highlight the impact of number of poles on demagnetization and torque density, Fig. 1 compares the 8-pole design with a 4-pole design in which the inclined layers offer sufficient space to allow magnets to be fitted, with the layers suitably tapered toward the airgap. The demagnetization proximity for the two designs at the worst rotor position are illustrated where 160% of the peak current (approximating the peak short circuit current) is applied in negative d-axis, while the red color indicates the areas prone to demagnetization; it is shown that, whilst the 8-pole design is safe from demagnetization the 4-pole design is heavily at risk.

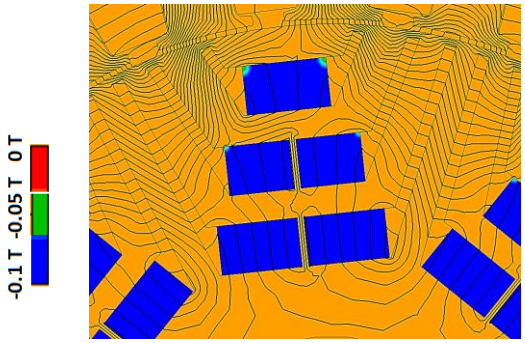

(a)

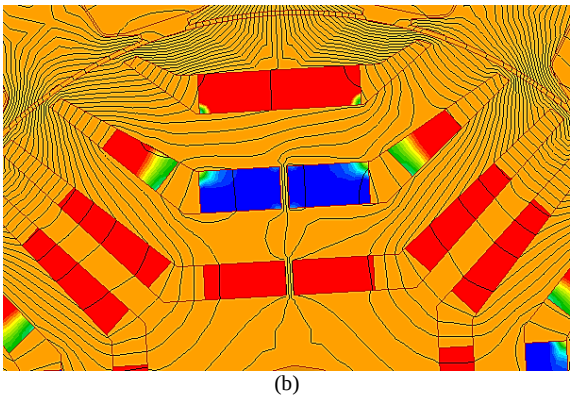

(b)

Fig. 1. Demagnetization proximity, PMASynR U-shape designs with ferrite magnets. (a) 8-pole design. (b) 4-pole design.

The torque vs. speed characteristic of the 8-pole design is calculated and shown in Fig. 2; it can be noted that for the

available volume the optimized design cannot fulfil the required peak torque at low speeds and, with larger deficit, the required constant power range from base to top speed. To highlight that it is the weak ferrite magnets which result in the lower than required performance, they are substituted with strong NdFeB magnets (Br equal to 1.2 T at 20˚C and Hcj equal to 1000 kA/m at 100˚C), with no other change in the design. The torque vs. speed characteristic is again shown in Fig. 2; it can be seen that, in contrast to the design with ferrite magnets, the 8-pole design with rare-earth magnets is able to exceed the constant torque and constant power range requirements.

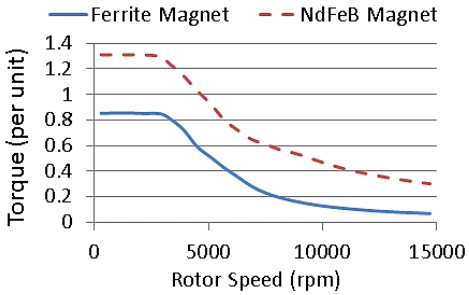

Fig. 2. Torque-speed performance of 8-pole PMAsynR design with ferrite and NdFeB magnets.

Another viable rotor topology is a three layer V-shape design, similar to that reported in [15]; in this topology, as an advantage over the U-shape alternative, the flux concentration with a high pole number configuration can still be achieved. However, it can be shown that, for U-shape and, more significantly, V-shape PMASynR topologies, to obtain a high ratio of reluctance torque and to avoid excessive saturation of rotor material, the rotor mass and the associated stress at high speeds will significantly be increased. To mitigate the rotor structure stress at high speeds, the rotor posts and bridges have to be significantly widened, which in turn leads to excessive flux leakage and torque loss. On this basis, although a three layer V-shape design may fulfill the required torque density at low to medium speed range (such as in [15]), it may not fulfil the high power density requirement in Table I.

In comparison to PMAsynR, the spoke type rotor design provides more space for magnets per given motor outer diameter (OD) thus allowing a higher number of poles without compromising the flux concentration effect; in addition, with this topology, significant reluctance torque can still be achieved. The topology also allows for demagnetization control via appropriate design of rotor pole tips and appropriate magnet placement between the poles. Finally, unlike the PMASynR solution which is based on a single piece rotor lamination, in a spoke type topology the posts and bridges may be fully or partially eliminated by employing a two part fir-tree based rotor structure; as a result, the speed and power density of the spoke type design can significantly be increased without a compromise on the flux leakage and performance.

Based on a multi-physics based optimization, Fig. 3, performing several iterations between electromagnetic and structural FE design packages, an optimal spoke type design with distributed winding (slots per pole and phase, q, equal to 2) has been achieved. The design cross section is shown in Fig. 4, and some key dimensions are reported in Table II. Some of the major steps during the design optimization procedure, see Fig. 3, can be summarized as follows: a) The number of poles has been maximized (limited by the maximum fundamental frequency of 1.25 kHz allowed by the inverter) to reduce the stress, via reduction of mass per pole, and demagnetization risk, via reduction of ampere turns per pole; b) The magnets radial height has been maximized (limited by the rotor mass and maximum stress allowed based on the structural analysis) to maximize the torque and power density; c) The circumferential width of the magnets was maximized (limited by the available space for the fir tree inclusion and the deviation from optimal ripple torque) to reduce the demagnetization risk; d) The open and rectangular slot configuration is chosen to maximize the torque density and to allow for the use of wires with rectangular cross section (to increase the slot fill factor and minimize the winding loss).

The rotor of the design in Fig. 4, is comprised of 5 axial sections, facilitating the rotor assembly, and enabling skew. The rotor support is made of non-magnetic steel due to its optimal structural properties and low costs, while the rotor poles are made of the same material as the stator laminations to improve the raw material utilization and achieve further cost savings.

It should be noted that in Fig. 3, only some of the fundamental optimization steps have been reported; the more detailed design considerations such as demagnetization and rotor structural design will be discussed in the following sections, while some other design aspects will be the scope of separate publications.

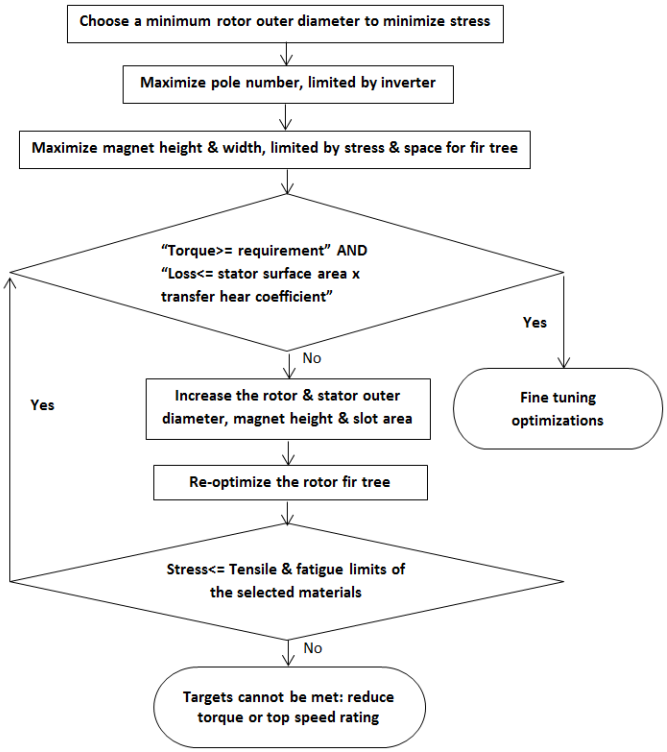

Fig. 3. Design optimization algorithm of the spoke type design.

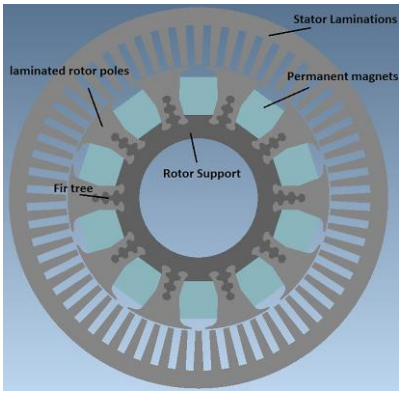

Fig. 4. A cross section of the optimized spoke type design.

TABLE II
Major dimensions of the spoke type design.

Stator outer diameter (mm)	205
Rotor outer diameter (mm)	140
Stack length (mm)	195
Airgap (mm)	0.5

C. Electromagnetic Analysis

1) Electromagnetic torque and efficiency map

The peak transient torque waveforms of the spoke type design corresponding to the base and top speed are shown in Fig. 5, where the torque and corresponding power marginally fulfill the requirements in Table I. To reduce the ripple torque however, the rotor is skewed by one full slot pitch, i.e. each rotor slice is shifted by 1.2 degree, as a result of which the ripple is reduced by factor of 2~3 as shown in Fig. 5.

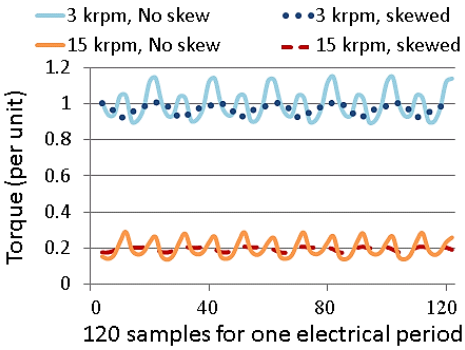

Fig. 5. Peak transient torque waveforms at base and top speed, with and without skew.

The windings loss (copper with 45% fill factor) and the iron loss, including stator and rotor laminations, for the peak torque/ power operation vs. speed are shown in Fig. 6(a); the per unit values are with reference to the maximum power output of the motor, i.e. 80 kW. It should be noted, that due to the high electrical resistivity of the ferrite magnets, these magnets do not contribute to any loss, regardless of the operational conditions; furthermore, the eddy current loss in the rotor support is negligible (equal to, only, 0.0001 per unit at the worst operating condition) owing to the distributed winding and the low rate of flux variation in the support region. As shown in Fig. 6(a), for the maximum torque operation, the winding loss dominates the iron loss for, almost, all the speed range.

To assess the total loss and efficiency for all operating conditions, the efficiency map as well as two representative key operating points (i.e. the points at which the motor frequently operates: one corresponding to urban driving, and one corresponding to highway cruising) are shown in Fig. 6(b). It can be realized that the efficiency of the design at both of the key operating points is above 95%, which is comparable to the state of the art designs with rare earth magnets, [22]. Furthermore, it can be shown that the iron loss exceeds the winding loss and becomes dominant at lower range of torque and higher range of speed, including the key operating points in Fig. 6(b). The major reasons behind the achieved level of high efficiency can be summarized as: a) high airgap flux density due to flux concentration, which results in less required armature current and winding loss for a given power, b) lossless ferrite magnets in rotor, c) distributed winding, d) despite the open slot configuration the width of the slot relative to the magnets is, rather, small owing to the high number of poles.

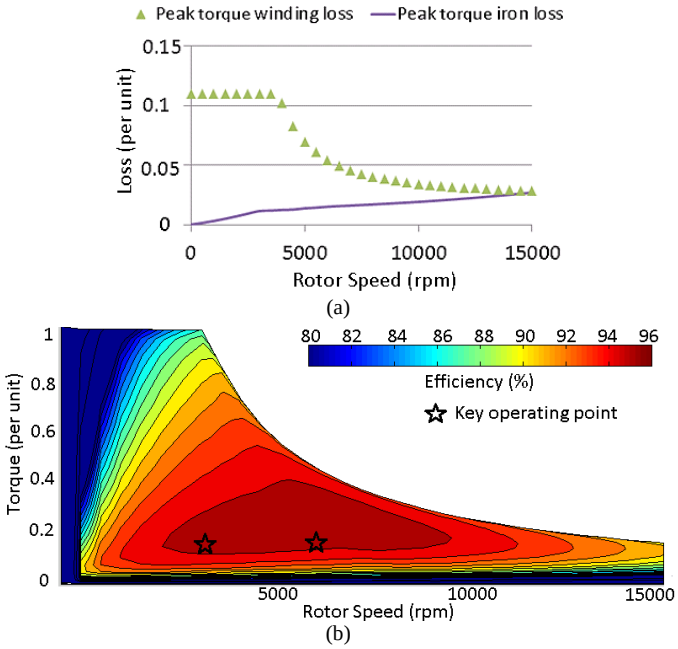

Fig. 6. Loss and efficiency map of the proposed spoke design. (a) Winding and iron loss for peak power operation. (b) Efficiency map.

2) Demagnetization

Ferrite magnets have approximately one fifth to one third of the coercivity, H_{cj}, of the rare earth magnets; for example a value of 330 kA/m in FB9B Ferrite at -40˚C compared to 900-1600 kA/m in NdFeB magnets at 100˚C. Furthermore, in an EV application with a high constant power to speed ratio, such as presented in this paper, currents almost as large as the peak current, i.e. 1 per unit, may be applied in the negative d-axis due to very high current advance angles applied at higher speeds. Even more critically, during short circuit faults negative d-axis currents with larger amplitude than the peak current can develop, against which the magnets need to be able to retain their full magnetic properties.

To avoid demagnetization in the presented spoke design, several design aspects have been observed: a) the number of poles is maximized following the explanation in chapter B; b)

the magnets are given adequate thickness in the circumferential direction to increase the magnetic reluctance in the d-axis; and c) the rotor ferromagnetic pole tip on top of the magnets (in a semi-open bridge configuration) is given adequate radial thickness and circumferential extension to encourage and bypass the stator d-axis fields during the extreme field weakening or short circuit faults.

A design solution whose merit is less apparent in the rare-earth magnet based designs, but which is crucial in the case of ferrite magnets, is to assign a non-magnetic void not only to the top, as proved effective in [16], but also to the bottom of the magnets as shown in Fig. 7(a) for a rather simplified model (the semi-open bridge in the actual design is approximated by a radially thinner full-bridge). These voids provide a leakage path for both the d-axis armature fields and magnet flux. The voids enable the armature and magnet to form two decoupled magnetic circuits whereas, were no voids allowed for, they would form a series coupling as a result of which the magnets would have to face the strong and negative fields from the armature and therefore higher risk of demagnetization. To highlight the suitability and necessity of this approach, in Fig. 7(b) the bottom void, and in Fig. 7(c) both top and bottom voids have been removed; furthermore, in Fig. 7(d) the bridge thickness is increased from 1 mm to 2 mm as an attempt to compensate the void removal. The demagnetization proximity is illustrated for a 160% peak current applied in the negative d-axis (resembling the peak short circuit current), where red zones illustrate the areas that will be demagnetized. As shown, removing the voids (Figs. 7(b) and 7(c)) significantly deteriorates the ability of the magnets to withstand demagnetization, while doubling the bridge thickness only provides marginal improvement (Fig. 7(d)). Furthermore, while thickening the bridge (e.g. Fig. 7(d)) significantly deteriorates the torque capability of the motor due to excessive leakage during the normal operation, the provision of non-magnetic voids would have negligible impact as is demonstrated in Fig. 8; this shows how the assisting role of the latter come into effect only during the rise of strong and negative d-axis fields.

In the case of the proposed design in Fig. 4, the aforementioned voids are accommodated via the non-magnetic rotor support at the bottom, and the non-magnetic wedge at the top; both with appropriate thicknesses inspired from Fig. 7. The inclusion of wedge also mitigates the risk that fragments of magnetic material are able to enter the airgap region. To fully assess the design, a 3-phase short circuit, initiated with the motor operating at base speed and at peak regenerative torque, is simulated in FE. The resulting currents are displayed in Fig. 9 (fault occurring at t=4 msec), indicating the peak short circuit current occurring in Phase A and equal to 1.6 times the rated peak current. The field strength (H) and flux lines corresponding to the most extreme rotor position are displayed in Fig. 10. Here, the maximum field strength in the magnet is close to the bottom surface and is about 300 kA/m, which is 10% lower than the H_{cj} of ferrite magnets at -40˚C. Furthermore, following the earlier explanation of the impact due to the inclusion of the voids, the field strength is largest near the airgap and rotor pole tips on top and bottom of the magnet but decays radially in the voids approaching the magnet's top and bottom surface. The magnet flux can be seen to leak primarily through the void beneath the magnet, while the armature flux leaks partially through the rotor pole tips and more significantly through the top and bottom voids.

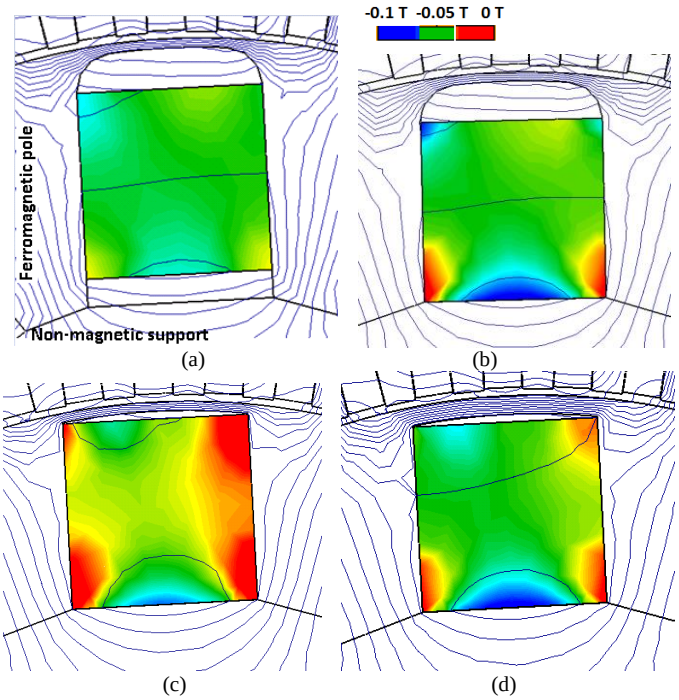

Fig. 7. Demagnetization proximity. (a) 1 mm bridge, 4 mm and 3 mm top and bottom air voids. (b) 1 mm bridge, 4 mm top air void, no bottom air void. (c) 1 mm bridge, no air voids. (d) 2 mm bridge, no air voids.

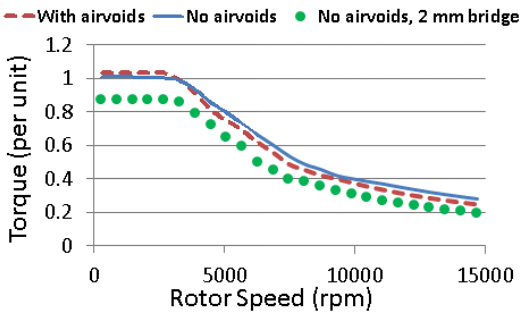

Fig. 8. Torque-speed comparison for designs with/ without air voids and different bridge thicknesses.

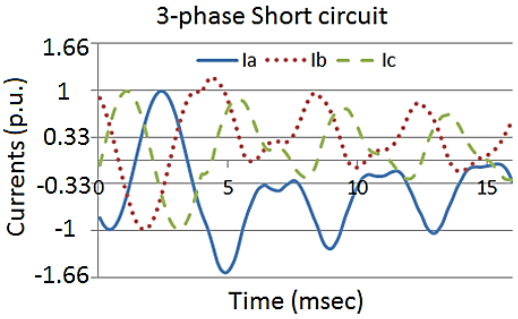

Fig. 9. 3-phase short circuit currents.

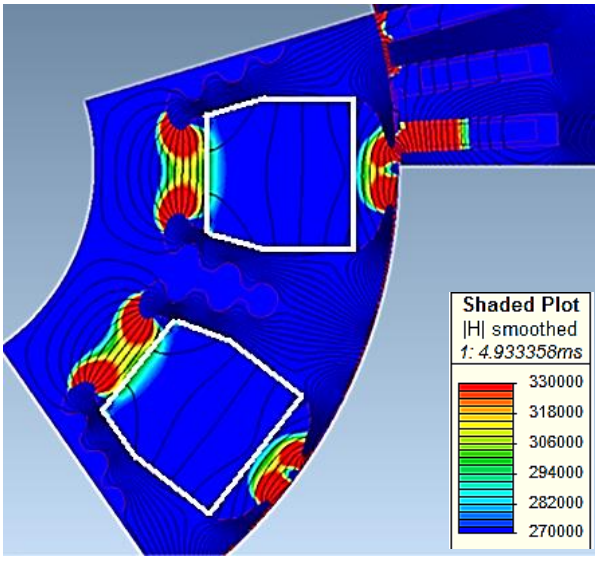

Fig. 10. Field strength (A/m) distribution during 3-phase short circuit.

Finally, the impact of the inclusion of a stator tooth tip on demagnetization has been studied. It has been observed to have an impact comparable to the rotor bridge, both in terms of providing limited protection against demagnetization as well as resulting in the potential for a loss of performance.

D. Rotor Structural Analysis

To hold the rotor poles and magnets to the non-magnetic rotor support at high speeds, a so-called fir-tree connection was adopted, Fig. 4. It can be shown that the torque density of the spoke design is proportional to the radial height of the magnet, which itself is limited by the increase of mass in the rotor pole and magnets and thus the stress in the rotor pole segments and support. To meet the torque requirement in Table I, by achieving the required magnet height in Fig. 4, several fir-tree configurations have been investigated through 2D elastic-plastic FE structural analysis. This analysis has included optimization against excessive rotor plastic deformation and radial expansion at maximum working speed (15,000 rpm), as well as against fatigue failure due to rotor speed changes. To design against fatigue failure, the analysis aims at an infinite fatigue life for the most severe rotor operating cycle, that is, a fatigue stress range resulting from the largest rotor speed variation possible (between 0 rpm and 15,000 rpm) for the entire life time of the vehicle.

Fig. 11(a) shows an early design (only half of a pole segment is shown due to symmetry) in which a high number of fir tree teeth have been chosen to efficiently distribute the mechanical loading. In addition, two circular cavities have been incorporated in the upper part of the pole to reduce the pole mass and thus the stress at high speeds. As indicated in Fig. 11(a), a number of design variables were examined during the optimization to minimize the stress concentrations at high speed: a) increasing the radius of the bubble cut-out connecting to the upper-most fir-tree tooth and smoothing the curvature, b) reducing the height of the lower fir-tree teeth, and c) enlarging the radius and smoothing the curvature of the bottom fir-tree shoulder.

The stress distribution in the initial design, Fig. 11(a), is obtained by FE and is shown for the maximum working speed of 15 krpm in Fig. 12. It can be observed that: a) The maximum stress in the rotor pole is almost evenly distributed with the maximum occurring at the top of the bubble cut-out indicating a need to further enlarge the corresponding bubble radius, and b) Stress on the support is significantly higher than on the poles, thus requiring a stronger material, for which 316 stainless steel with 3% work hardening is selected (this option is about 5 times cheaper than copper beryllium chosen in [19]). Meanwhile, the peak loading occurs in the fir-tree bottom shoulder which requires larger radius and further smoothing.

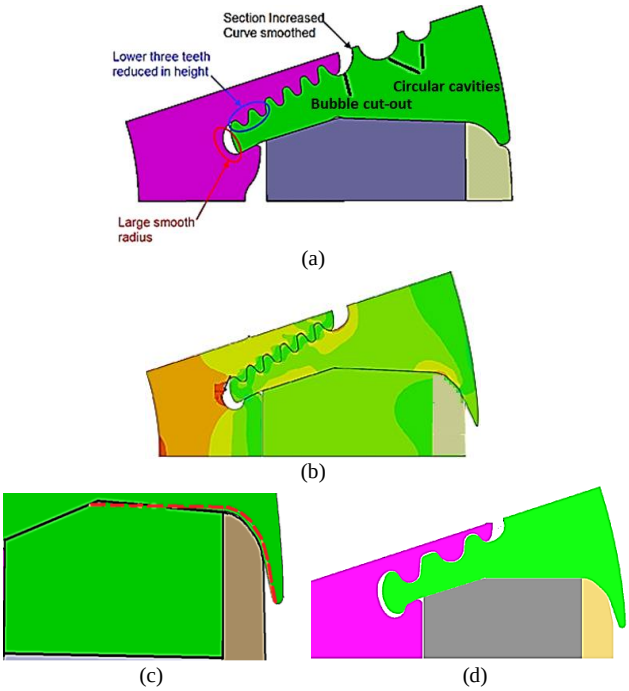

Fig. 11. Evolution of the rotor structural designs. (a) Initial design. (b) Top cavities removed. (c) Parallel vs. tapered face magnets. (d) Number of teeth reduced.

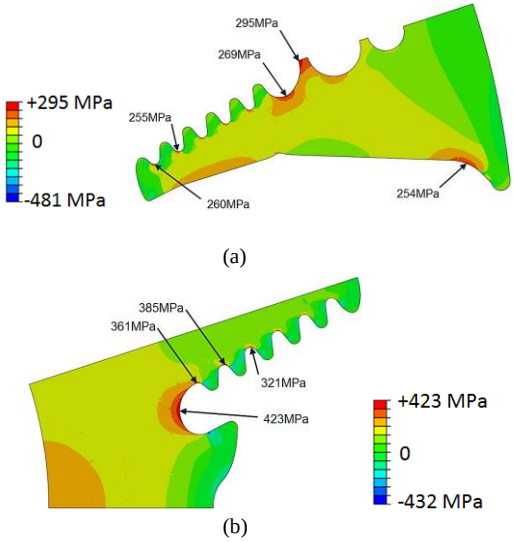

Fig. 12. Stress distributions at 15 krpm, initial fir-tree design. (a) Rotor pole. (b) Rotor support.

The two circular cavities in the pole segment of the fir tree design in Fig. 11(a) were found to deteriorate the magnetic performance by reducing the magnet torque (due an increase in the reluctance in front of the magnets) and also via a reduction in the reluctance torque, this being due to a reduction of the q-axis inductance. Furthermore, it was realized that a careful extension of the rotor pole tips could enhance the demagnetization withstand capability. As a result, in the subsequent design iteration, Fig. 11(b), the cavities are removed, and the pole tips extended, while fir-tree geometry improved accordingly to reduce the maximum stress levels.

To enhance manufacturability, however, the number of fir-tree teeth is reduced from 6 to 3 in a later design; there was concern that a large number of small teeth would be sensitive to small variations in manufacturing tolerances. Furthermore, through parts procurement, it was realized that the required manufacturing tolerances for the relatively complex ferrite magnet geometry were difficult to achieve. Through a simplification of the geometry, having a simpler shape with parallel magnet faces instead of tapered ones, as is shown in Fig. 11(c), better dimensional tolerances could be achieved. As a result, the final design, Fig. 11(d), was based on several modifications to accommodate both the reduced number of fir tree teeth and the extra loading on the pole segment as a result of eliminating the tapering of the magnet faces. The stress distribution for the final fir-tree design at the maximum working speed of 15 krpm is shown in Fig. 13. As shown, by modifying the rotor structural design from Fig. 12 to Fig. 13, the peak stress is reduced by about 15% in the pole segment and 24% in the rotor support.

It should be noted that, despite the similarities of the fir tree topology of Fig. 13 to that in [19], the former benefits from about 30% lower stress in the pole segment and 50% lower stress in the rotor support at a same top speed; the difference is majorly due to the optimization guidelines described and followed in this chapter. As a result, in the disclosed design, a substantially cheaper rotor support material has been employed, while, for a similar level of fatigue and product life time, higher speeds and power densities can be achieved.

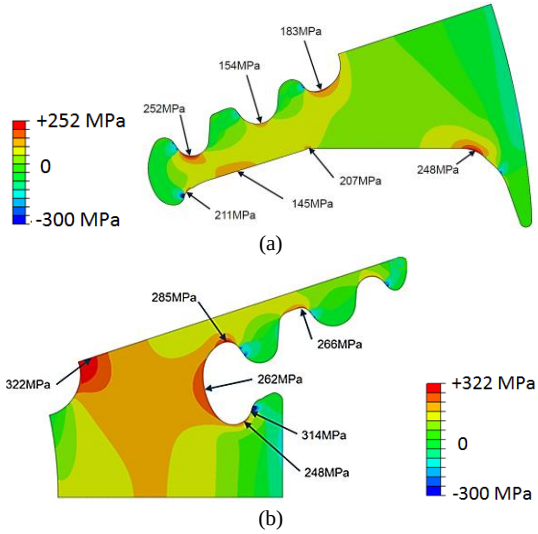

Fig. 13. Stress distributions at 15 krpm, final fir-tree design. (a) Rotor pole. (b) Rotor support.

E. Manufacturability for Mass Production

Due to the two-part rotor structure of the proposed design, the required geometrical tolerance of the fir tree (as a joint between the rotor support and the rotor pole) must be, finely, respected to avoid interference fitting problems during the assembly processes. As a result, to facilitate the assembly process for the mass production, the rotor parts should be checked against the specified geometrical drawings during the parts manufacturing procedure and as part of the quality control stage.

The necessity for a high quality manufacturing process might imply a certain cost increase when comparing the proposed two-part rotor design against the single piece alternatives, such as [18]; however due to the, significantly, better performance of the two-part rotor topology (owing to the less electromagnetic leakage than that in the single piece alternative), and due to the fact that the aforementioned manufacturing and quality control costs may be, significantly, reduced for a high volume production (as opposed to one off or low volume production), it has been realized that the proposed ferrite rotor design would maintain its favorability in terms of performance per cost.

III. PROTOTYPE AND TEST SET-UP

The two objectives of the testing described in this paper have been to assess the electromagnetic torque and demagnetization withstand capability of the proposed ferrite magnet motor design. On this basis, the prototype machine is simplified in several areas: a) The stack length is reduced to one fifth, to include only one of the five rotor sections as shown in Fig. 14(a), i.e. skewing is neglected, b) To measure the static torque only two coils of a single phase have been wound in the stator, as shown in Fig. 14(b), c) Due to procurement challenges, FB9B magnets were replaced by weaker but more readily available grade of ferrites, i.e. Ceramic 8, with B_r equal to 0.37 T and H_{cj} equal to 260 kA/m both at 20˚C, d) No cooling arrangements have been made for this prototype; thus to avoid temperature rise and/or overheating, each current injection was limited in duration to last no more than 2 seconds. Time taken to adjust and fix the rotor position between each injection meant that all results correspond to a winding temperature of ~20˚C. The test bed is shown in Fig. 15.

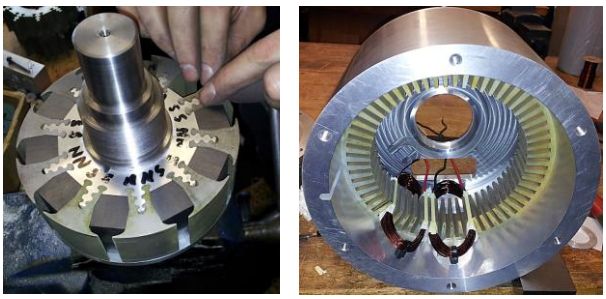

Fig. 14. Simplified prototype motor. (a) Rotor and magnets, (b) Stator, coils and custom built housing without cooling,

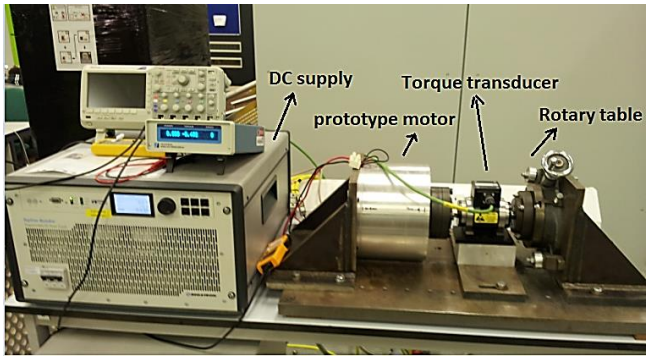

Fig. 15. Prototype test set-up.

IV. Test Results

A. Back-EMF (BEMF) and Static Torque Tests

The BEMF induced in one of the two coils of the prototype motor is measured at a fixed speed and compared to the 2D FE model which was set-up for the same conditions and the magnet grade explained in section III. To simplify the comparisons, the peak value of the FE predicted BEMF in Fig. 16(a) is defined as 1 per unit throughout this chapter. As shown in Fig. 16(a), the measured BEMF is about 8% lower (fundamental component calculated from FFT) compared to the 2D FE prediction, which may be largely attributed to the leakage of magnet flux in the end regions. However, it should be noted that since the stack and magnets axial length in the actual design are 5 times longer than the test prototype, the end leakage ratio in the full size machine will be significantly lower.

The static torque for different magnet / armature alignments is measured with a torque transducer, with rotor angle fixed through the use of a rotary table, Fig. 15. An identical model was set-up and simulated in 2D FE, and the results of the simulation and measurement are compared in Fig. 16(b). The two curves show very close agreement in terms of torque variation against the rotor position which can be looked upon as the advance angle. However, the peak torque from the prototype is about 9% smaller than the 2D FE prediction, which is a similar ratio as the BEMF reduction, and is attributed to the same phenomenon, i.e. magnet end leakage. Similar to the comments on the BEMF, the relative loss of torque would be expected to be significantly lower for a full size machine.

By scaling the results in Fig. 16(b) to the full motor size and assuming the actual grade of magnet (a total scaling factor of 29 may be used), it can be concluded that the proposed design can deliver a peak torque and power density of up to 19 Nm/liter and 6 kW/ liter (based on a 14 liter gross volume including the cooling housing and end windings, and a base speed assumption of 3000 rpm) which, marginally, fulfil the requirements in Table I. A full scale prototype and different test facilities are, currently, under construction to undertake a series of multi-physics (electromagnetic, thermal, and structural) testing at different torque-speed operating conditions.

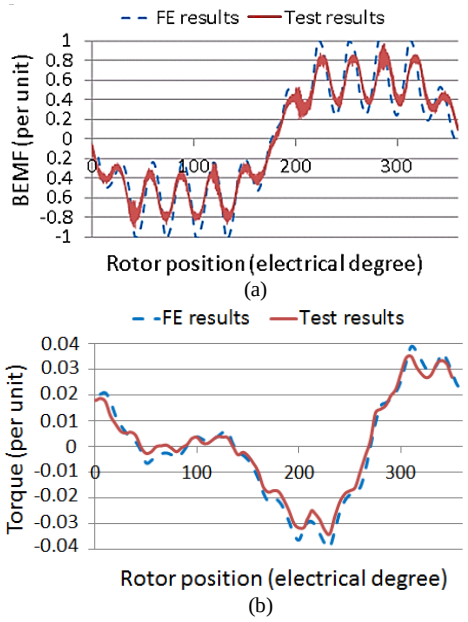

Fig. 16. Motor performance, comparison between measured and FE calculations. (a) BEMF. (b) Static torque vs. different rotor angles.

B. Demagnetization Test

To assess the demagnetization withstand capability of the design, currents with 160%, 200% and 240% of the peak current amplitude, i.e. 1 per unit, are injected in the negative d-axis. To accommodate all three current injections in a single test and provide a clear comparison, three magnets were subjected to different demagnetization fields, as shown in Fig-17. Once the demagnetization fields have been applied, the BEMF for one mechanical revolution of the rotor is then measured at the same speed as for the previous BEMF tests. The result is shown and compared, in Fig. 18, against the BEMF prior to demagnetization test. As shown, neither the magnet experiencing 160% of the peak current (resembling the peak short circuit current), nor the one exposed to 200% of the peak current is demagnetized, and the associated BEMF waveforms, therefore, are unchanged. On the other hand, the magnet associated with 240% of the peak current is partially demagnetized and the relevant BEMF is reduced by 12%, as indicated in Fig. 20.

To better understand the results, a similar demagnetization scenario was modelled in 2D FE. The predicted demagnetization is illustrated in Fig. 19, the red areas indicating the field strength greater than or equal to 260 kA/m and the magnet regions that will be demagnetized. In a further assessment, the demagnetized areas were replaced by air and the modified FE models were run at the same RPM as that of the measurement. The simulated BEMF values (fundamental components) are compared against those from measurement in Fig. 20. It is interesting to note that the 2D FE model prediction is significantly more pessimistic than the measurement. This can mostly be attributed to the relatively short length of the prototype which allows for higher end leakage from the coils as well as the magnets. This phenomenon is expected to lower the magnetic coupling between the armature and the magnets, leading to a better demagnetization withstand capability in total. On this basis, it

is expected that for the actual model with five times larger stack length the demagnetization behavior will be worse than the measured values and closer to 2D FE predictions. A 3D FE analysis of this phenomenon is intended and will be addressed in a separate paper.

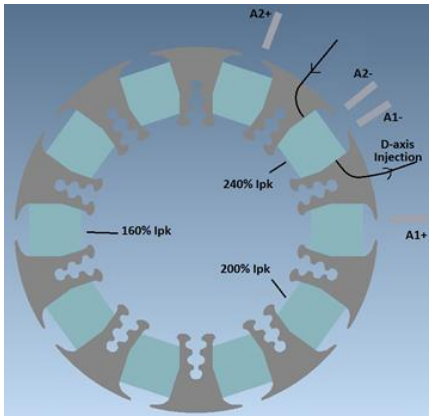

Fig. 17. Demagnetization test configuration.

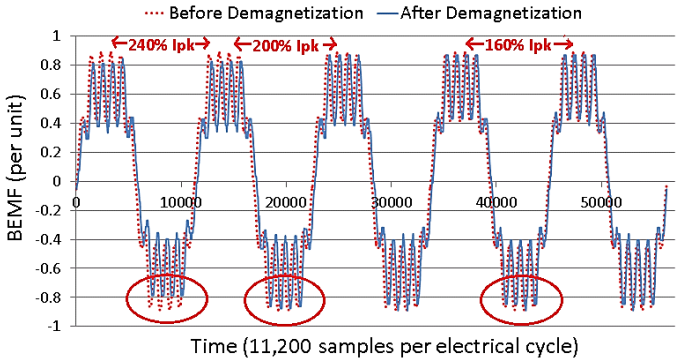

Fig. 18. BEMF before and after negative d-axis current injections.

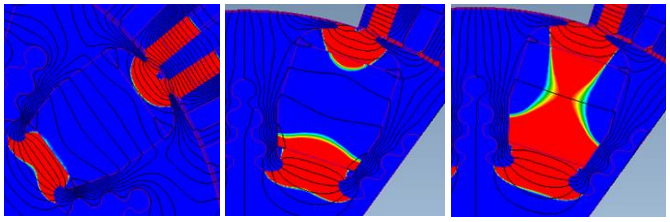

(a) (b) (c)

Fig. 19. 2D FE predicted demagnetization (H) with different current amplitudes applied in negative d-axis. (a) 160% I_{pk}. (b) 200% I_{pk}. (c) 240% I_{pk}.

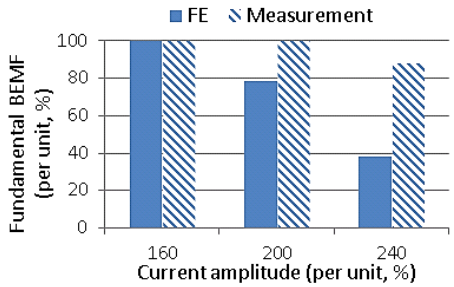

Fig. 20. Loss of BEMF fundamental component due to demagnetization; prototype measurement compared against 2D FE.

It has not been possible to test rotor demagnetization at low temperatures (-40 ˚C) at this stage. However the small scale prototype shows a stronger demagnetization resistance capability than the FE predictions, Fig. 20, at room temperature. FE modelling, as shown in Fig. 10, has also been undertaken assuming the ferrite magnet's coercivity at -40 ˚C, which suggests that the design will be robust at these low temperatures. The objective is that this will be proven experimentally in the future.

V. Conclusion

An optimized ferrite magnet based electrical machine design was presented for a high power density EV application. From different rotor topologies, the spoke type is explained to be the best suited, due to a simultaneous potential for obtaining high torque density, high demagnetization withstand capability, and a robust rotor structure for high speed operation. The resistance to demagnetization is optimized via a combination of techniques, namely: having a high number of poles; shaping and extending the rotor pole tip; widening the magnets; and most significantly, by incorporating the non-magnetic voids on the top and bottom of the magnets. The required torque density was achieved by maximizing the radial height of the magnets, enabled through an extensive optimization of the fir-tree design. The detailed optimization of the rotor structure resulted in substantially lower stress levels compared to the state of the art, based on which the product cost has been reduced, while the opportunity for further increase of the top speed and power density was revealed. A simplified test set-up is prepared and customized for BEMF, static torque and demagnetization assessments. Based on the measurements taken, the torque density of the design was about 9% lower than FE predictions; however, the demagnetization withstand was significantly better than FE predictions. It was explained that the deviations between the measurement and the 2D FE simulations are due to the relatively short stack length of the test prototype and will be diminished for the actual full size design. The disclosed motor design is claimed to surpass the state of the art in terms of performance (power density, demagnetization withstand capability, and rotor integrity) and cost; it is expected that this paper provides a better understanding of the interactions between the electromagnetic, structural and manufacturing issues involved within a cost effective industrial product.

References

[1] J. D. Santiago, H. Bernhoff, B. Ekergårdet, *et al.*, "Electrical Motor Drivelines in Commercial All Electric Vehicles: a Review'', IEEE Trans. Vehicular. Tech., vol. 61, no. 2, pp 475-484, Feb. 2012.

[2] T. A. Burress, S. L. Campbell, C. L. Coomer, *et al.*, "Evaluation of the 2010 Toyota Prius Hybrid Synergy Drive System,'' Oak Ridge Nat. Lab., Oak Ridge, TN, USA, ORNL/TM-2010/253, Mar. 2011.

[3] R. H. Staunton, T.A. Burress, and L.D. Marlino, "Evaluation of 2005 Honda Accord Hybrid Electric Drive System,'', Oak Ridge Nat. Lab., Oak Ridge, TN, USA, ORNL/TM-2006/535, Sep. 2006

[4] Y. Sato, S. Ishikawa, T. Okubo, *et al.*, "Development of High Response Motor and Inverter System for the Nissan leaf electric Vehicle'', SAE Technical Paper 2011-01-0350, Apr. 2011.

[5] G. Pellegrino, A.Vagati, P. Guglielmi, *et al.*, "Performance comparison between Surface Mounted and Interior PM motor drives for Electric Vehicle application,'' IEEE Trans. Ind. Electron., vol 59, pp 803 – 811, Feb. 2012.

[6] S. Morimoto, S. Ooi, Y. Inoue, and M. Sanada, "Experimental Evaluation of a Rare-Earth-Free PMASynRM With Ferrite Magnets

for Automotive Applications,'' IEEE Trans. Ind. Electron., vol. 61, no. 10, Oct. 2014.

[7] K. I. Laskaris, "Internal Permanent Magnet Motor Design for Electric Vehicle Drive,'' IEEE Trans. Ind. Electron., vol. 57, no. 1, pp 138-145, Jan. 2010.

[8] T. Jahns, "Flux-weakening regime operation of an interior permanent magnet synchronous motor drive, '' IEEE Trans. Ind. Appl., vol. 23, no. 4, pp. 681-689, July. 1987.

[9] Electric Motors 101: Understanding the Basics of Electric Motor Technology, pp 1-5. General Motors. [Online]. Available: www.gmgoelectric.com

[10] Electrical drive motor for a vehicle, by J. Merwerth, J. Halbedel, and G. Schlangen. (2012, Oct). Patent US 2012/0267977. [Online]. Available:file://tower6/home33/nmk62/Downloads/US20120267977.pdf

[11] A.M. EL-Refaie, J. P. Alexander, S. Galioto, *et al*., "Advanced High Power-Density Interior Permanent Magnet Motor for Traction Applications'', Accepted to be published in IEEE Trans. Ind. Appl., 2014.

[12] S. Constantinides. (2010, Dec). The Magnetic Material Challenge. Arnold Magnetic Technologies. [Online]. Available: www.arnoldmagnetics.com/

[13] S. Chu. (2011, Dec). Critical Materials Strategy. US Department of Energy (DOE). [Online]. Available: http://energy.gov/

[14] D. Dorrel, L.Parsa, and I.Boldea, "Automotive Electric Motors, Generators, and Actuator Drive Systems With Reduced or No Permanent Magnets and Innovative Design Concepts,'' IEEE Trans. Ind. Electron., vol. 61, no. 10, Oct. 2014.

[15] H. Cai, B. Guan, and L. Xu, "Low-cost ferrite PM-assisted synchronous reluctance machine for electric vehicles," IEEE Trans. Ind. Electron., vol. 61, no.10, pp.5741-5748, Oct. 2014.

[16] D. G. Dorrell, M. F. Hsieh, and A. M. Knight, "Alternative rotor designs for high performance brushless permanent magnet machines for hybrid electric vehicles," IEEE Trans. Magn., vol. 48, no. 2, pp. 835–838, Feb. 2012.

[17] S. I. Kim, J. Cho, S. Park, T. Park, and S. Lim, "Characteristics comparison of a conventional and modified spoke-type ferrite magnet motor for traction drives of low-speed electric vehicles," IEEE Trans. Ind. Appl., vol. 49, no. 6, pp. 2516-2523, Dec. 2013.

[18] Y. Burkhardt, A. Spagnolo, P. Lucas, *et al*., "Design and analysis of a highly integrated 9-phase drivetrain for EV applications," International Conference on Electrical Machines (ICEM), Sep 2014, pp. 450 – 456.

[19] S. J. Galioto, P. B. Reddy, A. M. EL-Refaie, "Effect of Magnet Types on Performance of High Speed Spoke Interior Permanent Magnet Machines Designed for Traction Applications,'' in Proc. IEEE ECCE, Sep. 2014, pp. 4513 - 4522.

[20] "Permanent Magnet Rotor for High Speed Motors and Generators,'' by Carl J. Heyne, Granted on May 1986, US4588914 A, Available: http://www.google.com.ar/patents/US4588914.

[21] (2011, June). Ferrite Magnets FB Series. TDK Magnetics. [Online]. Available: http://product.tdk.com/en/catalog/datasheets/e321.pdf

[22] S. A. Rogers, "Annual Progress Report, Advanced Power Electronics and Electric Motors Program," US Department of Energy, DOE/ EE-0864, Jan. 2013.